Composite Structures 291 (2022) 115540

Contents lists available at ScienceDirect

Composite Structures

journal homepage: www.elsevier.com/locate/compstruct

Elastic anisotropy and wave propagation properties of multifunctional hollow sphere foams

Zian Jia [a,*], Fan Liu [b], Ling Li [a], Lifeng Wang [b,*]

[a] Department of Mechanical Engineering, Virginia Tech, Blacksburg, VA 24061, USA
[b] Department of Mechanical Engineering, State University of New York at Stony Brook, Stony Brook, NY 11794, USA

ARTICLE INFO

Keywords:
Architected multifunctional materials
Hollow sphere foams
Direction-dependent properties
Auxetic material
Complete band gap

ABSTRACT

Obtaining multifunctionality from microstructures instead of constituents provides a new direction for developing multifunctional materials. Periodic hollow sphere foams (HSFs) offer one lightweight structural motif with open and closed cells, high energy absorption, low thermal conductivity, snap-through instability, and triple-negative material indices. Here, we investigate the direction-dependent mechanical property, instability, and elastic wave isolation behavior of HSFs. Explicit formulas, stereographic projections, and general scaling relationships are developed to quantify and visualize the anisotropic mechanical properties of HSFs. By investigating the directional wave propagation in HSFs, extremely wide phononic band gaps are identified in the HSFs. The derived formulas and the simulation-informed parametric maps allow the design of HSFs with desired static and dynamic anisotropic property profiles, including tailorable direction-dependent stiffness/shear modulus, negative Poisson's ratio, and wave isolation properties. Building upon these results, multifunctional design concepts of HSFs are further set forth. This study not only reveals tailorable mechanical anisotropy and band gap in HSFs, but also develops a general approach to investigate the direction-dependent properties of periodic materials, enabling multifunctional applications where lightweight, direction-dependent property, wave attenuation, and programmability are required simultaneously.

1. Introduction

Architected materials provide one approach to achieve multifunctionality by designing the material microstructure [1–6]. In recent decades, architected lattice materials have been shown to achieve remarkable mechanical, thermal, and acoustic properties, arising from their periodic microstructures [1,7–11]. By tailoring the unit cell geometry, lattice materials have been designed successfully to achieve property combinations that break performance tradeoffs [12,13], improve thermal and mechanical performance [14–16], produce negative material indices [17,18], acquire piezoelectric energy harvesting functionalities [19,20], and many others. Developing lattice materials with multiple of the above functions is highly in need. In this study, we propose periodic hollow sphere foam (HSF) as a lightweight material structural motif for multifunctionality.

HSF is a class of cellular lattice material that exhibits low density, large void space, and large specific surface area [21,22] (Fig. 1). It has both open and closed cells, which thus offers the advantages of open and closed cell foams simultaneously, including large surface area, enhanced stiffness, lower thermal conductivity, and buoyancy. In the past, random HSFs have been widely used in energy absorption [23], thermal management [24], fluid permeability control [25], and pressure sensors [26]. Filling metallic tubes with hollow spheres has been shown as an efficient way to improve the axial crushing strength of the tube; binding these hollow spheres can improve the crash-worthiness even further [27,28].

Recent advances in synthesis have enabled the assembly of hollow spheres into periodic foams with binding [29], sintering [30], and self-assembling processes [31,32]. Such periodic HSF lattices have well-defined material architecture and enable functions beyond that of traditional random foams. For example, the mechanical and thermal properties of periodic HSFs can be tailored by designing geometric parameters [15,33]. Periodic structures also give rise to unusual properties like band gaps [34–36] and negative material indices [17,37,38]. Phononic crystals with complete bandgap are important to applications like wave filters [39–42], waveguides [43–45], frequency modulators [46,47], acoustic cloaks [48,49], and thermal insulators [50]. Recently, by taking advantage of the snap-through instability of spherical shells,

* Corresponding authors.
E-mail addresses: zian@vt.edu (Z. Jia), Lifeng.wang@stonybrook.edu (L. Wang).

https://doi.org/10.1016/j.compstruct.2022.115540
Received 30 October 2021; Received in revised form 2 March 2022; Accepted 1 April 2022
Available online 9 April 2022
0263-8223/Published by Elsevier Ltd.

mechanical memory has also been devised, which enables programmable modulus and strength over an order of magnitude [51]. Fig. 1 provides an overview of the functionalities and applications of HSFs.

Applications of lattice materials in research fields like scaffolds for bone regeneration [19], substrates for tissue growth [52], multi-lattice structures [53], and metamaterials [1] have set additional requirements to designing a materials' anisotropic properties [54]. Simulations approaches have been used to plot the anisotropic modulus map of periodic lattices and composites [55,56]. It has been shown that truss-based lattice materials often exhibit high mechanical anisotropy; introducing redundant trusses and combining different lattices types provides one efficient way to adjust anisotropy and to achieve quasi-isotropic properties [54]; designing the structural morphology provides an alternative approach to tune anisotropy [57]. Moreover, in addition to static mechanical properties, the wave propagation properties of lattice materials are also direction dependent – waves of certain frequencies are often allowed to propagate in some directions but not in others [58].

In this study, we investigate the direction-dependent elastic and wave propagation properties of HSFs, aiming to introduce new functionalities to the functional library of HSFs (Fig. 1). Specifically, we first propose explicit formulas and adapt the stereographic projection method in crystallography to study the direction-dependent properties of lattice materials. Combining with numerical simulations, the anisotropic mechanical properties of HSFs arranged in simple cubic (SC), body-centered cubic (BCC), and face-centered cubic (FCC) lattices are studied systematically. Universal scaling equations are proposed to describe the elastic constants of HSFs and guide their quantitative design. The direction-dependent wave propagation properties in HSFs are further inspected. Finally, based on the direction-dependent properties shown herein, concept designs of HSFs as tailorable, adaptive, and programmable multifunctional materials are demonstrated.

2. Materials and methods

2.1. Structural description of the hollow sphere foams

As depicted in Fig. 1(a), HSFs are a periodic assembly of spherical shells connected by binders. The geometry of the HSFs is defined by four parameters, the radius of the hollow sphere, R, the thickness of the hollow sphere, t, the radius of the binder, r_b, and the height of the binder, h. Here, we limit the arrangement of hollow spheres to be cubic symmetric, i.e., in SC, BCC, and FCC lattices. The corresponding unit cells are shown in Fig. 2. As the unit cells consist of shells and binders, a first-order estimation of the volume occupied by HSF in a unit cell is $n{\cdot}4\pi R^2 t + m{\cdot}\pi r_b^2 h$, with n and m depict the numbers of shells and the numbers of binders in a unit cell, respectively. The total volume of the unit cell is proportional to R^3, so, the volume fraction of HSF can be evaluated as

$$V_f = At/R + B(r_b/R)^2 h/R, \tag{1}$$

where A and B are scaling constants that depend on the lattice type. When the binders are relatively small ($r_b \to 0$ or $h \to 0$), the volume fraction $V_f \propto At/R$, and the relative density of HSF is proportional to the relative shell thickness (t/R).

2.2. Mechanical simulation

Finite element simulations are carried out to obtain the elastic constants of the HSFs. For cubic materials, the elastic tensor is defined by three elastic constants, namely, Young's modulus E_{11}, Poisson's ratio ν_{12}, and shear modulus G_{12}. In the simulation, E_{11} and ν_{12} are evaluated by performing numerical uniaxial compression while G_{12} is obtained by performing numerical simple shear tests. To reduce the computational cost, the simulations are conducted on unit cells with periodic boundary conditions, as described in Fig. 2a [59] (see more details are in the supplementary materials). Specifically, the unit cell is subjected to a prescribed deformation defined by the deformation gradient $\mathbf{F}$, the displacements on pairs of points on the periodic boundaries are enforced to satisfy [59,60]

$$\mathbf{u}(B) - \mathbf{u}(A) = (\mathbf{F} - \mathbf{I})\{\mathbf{X}(B) - \mathbf{X}(A)\} = \mathbf{H}\{\mathbf{X}(B) - \mathbf{X}(A)\} \tag{2}$$

where A and B are paired points located on the opposite faces of the unit cell as illustrated in Fig. 2(a); $\mathbf{u}$ denotes the displacement, $\mathbf{X}$ denotes the

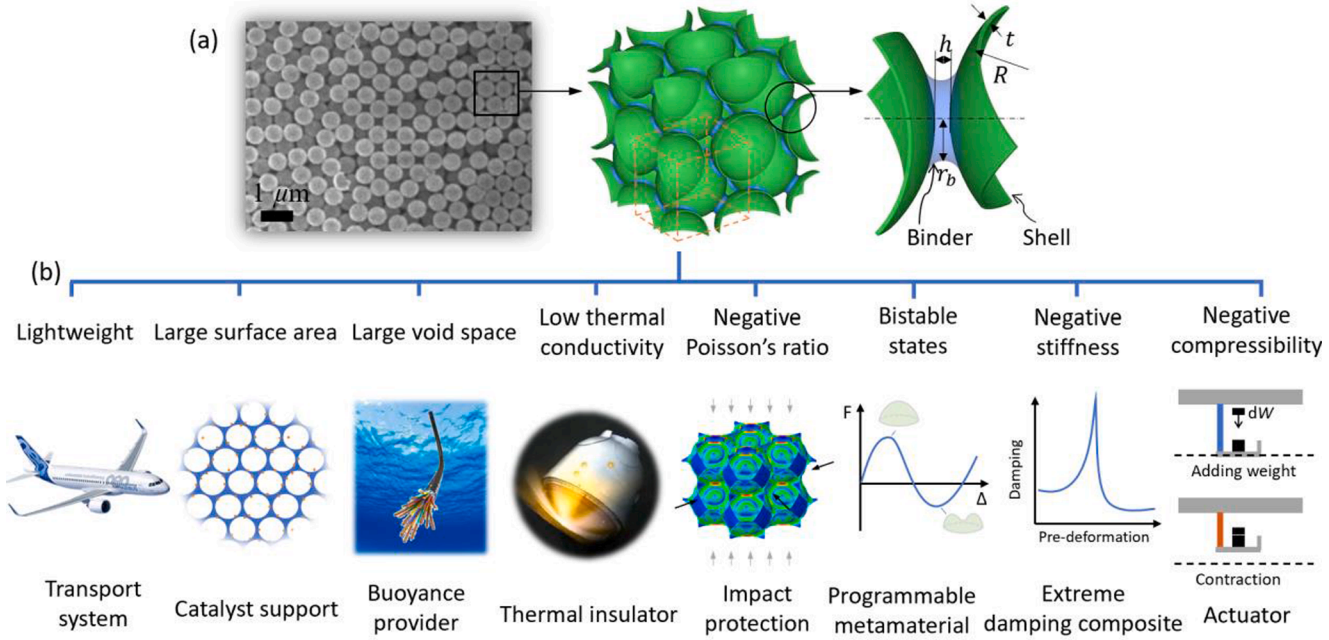

Fig. 1. Multifunctional properties of the hollow sphere foam (HSF) enabled by microstructure. (a) The geometry of HSFs is defined by R, t, r_b, and h. (b) The multifunctionality and corresponding applications of HSFs. The SEM image in (a) is reproduced with permission from Ref. [32]. Copyright 2012 American Chemical Society. The image panels of airplane and space capsule in (b) are acquired from open online resources.

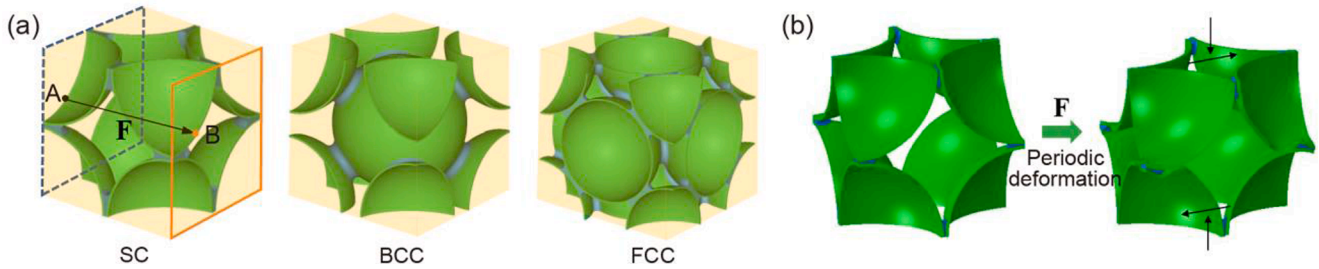

Fig. 2. (a) The unit cells and (b) the boundary conditions used to simulate the elastic properties of HSFs.

position in the reference configuration, and $\mathbf{H} \equiv \mathbf{F}\text{-}\mathbf{I}$ is the macroscopic displacement gradient tensor. Simulation is conducted in ABAQUS. $\mathbf{H}_{3\times3}$ is implemented by three reference nodes and the components of $\mathbf{H}_{3\times3}$ are assigned based on the loading condition. For uniaxial compression in the x-direction, H_{11} is assigned as the applied compressive strain (0.05 for evaluating elastic constants) while all the diagonal components of $\mathbf{H}$ are assigned to be zero. A representative mesh used in the simulation is shown in Fig. S1.

Based on the macroscopic response of the unit cell calculated from ABAQUS, E_{11}, ν_{12}, and G_{12} are calculated accordingly. Because the hollow spheres have thin features, their local strain is small under a compressive strain up to 0.13. Moreover, as the anisotropic elastic constants are defined by the small deformation regime of the HSF, elastic material models are used in the simulations. The material properties used in the simulation are $E_b/E_s = 0.04$, $\nu_b = 0.4$ and $\nu_s = 0.3$, representing aluminum or glass hollow spheres ($E_s = 70$ GPa) connected by polymetric binders ($E_b = 2.8$ GPa). The geometric parameters are $t/R = 0.03$, $r_b/R = 0.2$, $h/R = 0.02$ unless otherwise specified. The subscripts "b" and "s" refer to the binder and shell, respectively.

2.3. Formula and approach to visualize the anisotropic elastic properties of cubic materials

The elastic constants E_{11}, ν_{12}, and G_{12} describe the mechanical behavior of HSFs when loads are applied in the orthogonal directions (x_1, x_2, and x_3) of the reference coordinate system $\boldsymbol{x}$[Fig. 3(a)]. To visualize the mechanical properties of a material in arbitrary loading directions, a spatial coordinate system ($\boldsymbol{x}'$) is introduced. Because Young's modulus only depends on one direction – the direction of the load, thereby, its direction-dependent behavior can be visualized using a 3D elastic representative surface [Fig. 3(c)][61]. In contrast, Poisson's ratio (ν_{ij}) and shear modulus (G_{ij}) depend on two directions: the loading direction i and the second lateral direction j. For a specified loading direction i, direction j is defined perpendicular to direction i and varies

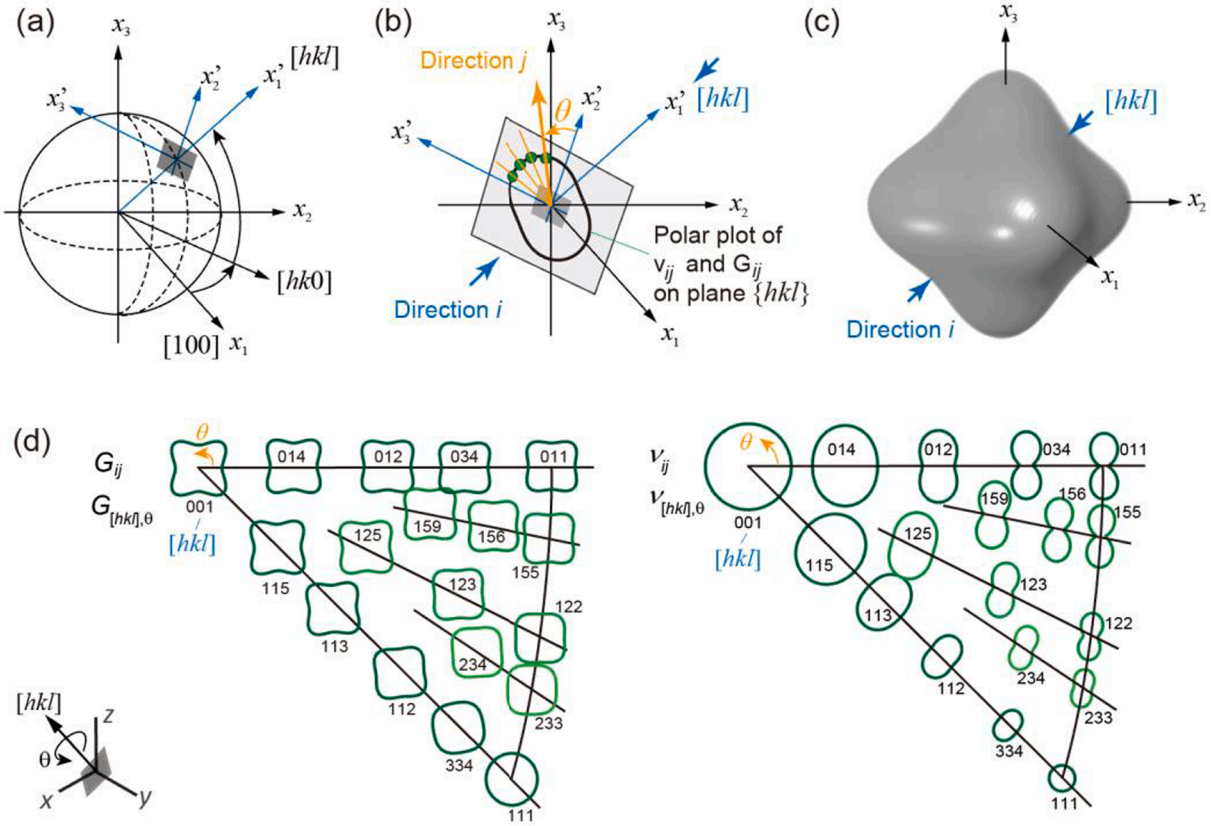

Fig. 3. Visualization of the direction-dependency of Young's modulus, Poisson's ratio, and shear modulus. (a) Definition of the reference and the spatial coordinate systems. (b) Illustration of the two directions ([*hkl*] and θ) used to define Poisson's ratio ν_{ij} and shear modulus G_{ij}. (c) Elastic representative surface describes material parameters that only depend on one direction (like Young's modulus $E_{[hkl]}$). (d) The triangle of the stereographic projection describes material parameters that depend on two directions (like Poisson's ratio $\nu_{[hkl],\theta}$ and shear modulus $G_{[hkl],\theta}$). The polar plots are drawn to scale.

in the range of $[0, 2\pi)$ [Fig. 3(b)]. Defining the directions i and j by $[hkl]$ and θ, respectively, we can generate a polar plot for each given $[hkl]$ as shown in Fig. 3(b, d). We have obtained formulas to depict elastic anisotropy previously in [33], here, we provide the detailed derivation for the completeness of this study.

For a cubic material, symmetry requires the elastic compliance tensor to have the following form [62],

$$S'_{ijkm} = S_{12}\delta_{ij}\delta_{km} + \frac{1}{4}S_{44}(\delta_{ik}\delta_{jm} + \delta_{im}\delta_{jk}) + (S_{11} - S_{12} - \frac{1}{4}S_{44})a_{it}a_{jt}a_{kt}a_{mt}. \quad (3)$$

where S_{ijkm} and S'_{ijkm} are the compliant tensor in the reference coordinate system (x) and spatial coordinate system (x'), respectively. The notation $a_{it}a_{jt}a_{kt}a_{mt}$ follows [62], which is defined as $\sum_{t=1,2,3} a_{it}a_{jt}a_{kt}a_{mt}$. The transformation matrix, a_{st}, has the following form,

$$a_{st} = \begin{bmatrix} \frac{h}{\sqrt{h^2+k^2+l^2}} & \frac{k}{\sqrt{h^2+k^2+l^2}} & \frac{l}{\sqrt{h^2+k^2+l^2}} \\ -\frac{\sqrt{k^2+l^2}\cos\theta}{\sqrt{h^2+k^2+l^2}} & \frac{hk\cos\theta}{\sqrt{k^2+l^2}\sqrt{h^2+k^2+l^2}} - \frac{l\sin\theta}{\sqrt{l^2+k^2}} & \frac{hl\cos\theta}{\sqrt{k^2+l^2}\sqrt{h^2+k^2+l^2}} + \frac{k\sin\theta}{\sqrt{l^2+k^2}} \\ \frac{\sqrt{k^2+l^2}\sin\theta}{\sqrt{h^2+k^2+l^2}} & -\frac{l\cos\theta}{\sqrt{h^2+k^2}} - \frac{hk\sin\theta}{\sqrt{k^2+l^2}\sqrt{h^2+k^2+l^2}} & \frac{k\cos\theta}{\sqrt{h^2+k^2}} - \frac{hl\sin\theta}{\sqrt{k^2+l^2}\sqrt{h^2+k^2+l^2}} \end{bmatrix}. \quad (4)$$

Combining Eqs. (3) and (4), S'_{ijkm} can be written in a general equation (with the Voigt notation S'_{ij}),

$$S'_{ij} = S_{ij} + A{\cdot}F_{ij}([hkl], \theta). \quad (5)$$

where $A = (S_{11} - S_{12} - \frac{1}{2}S_{44})$ is the anisotropic parameter. $F_{ij}([hkl], \theta)$ are functions of the direction vector $[hkl]$ and rotation angle θ. The expressions of F_{ij} are

$$F_{11} = -2\left(h^2k^2 + k^2l^2 + l^2h^2\right), \quad (6)$$

$$F_{12} = \frac{2}{k^2+l^2}\left[\left(k^4 + k^2l^2 + l^4\right)\cos^2\theta + hkl\left(l^2 - k^2\right)\cos\theta\sin\theta + k^2l^2\sin^2\theta\right], \quad (7)$$

$$F_{44} = \frac{4}{\left(k^2+l^2\right)^2}\left[\left(k^2+l^2\right)^4\cos^2\theta\sin^2\theta + \left(l\cos\theta + hk\sin\theta\right)^2\left(hk\cos\theta - l\sin\theta\right)^2 + \left(hl\cos\theta + k\sin\theta\right)^2\left(k\cos\theta - hl\sin\theta\right)^2\right]. \quad (8)$$

Based on Eqs. (5) and (6), Young's modulus of a cubic material in an arbitrary direction $[hkl]$ is derived,

$$\frac{1}{E_{[hkl]}} = \frac{1}{E'} = S'_{11} = \frac{1}{E_{[100]}} - 2A(h^2k^2 + k^2l^2 + l^2h^2). \quad (9)$$

Eq. (9) recovers the formula of elastic representative surface, which has been previously derived in Refs. [61,63]. Moreover, Poisson's ratio and shear modulus can be expressed as,

$$\nu_{[hkl],\theta} = -\frac{S'_{12}}{S'_{11}} = -\frac{S_{12} + A{\cdot}F_{12}([hkl], \theta)}{S_{11} + A{\cdot}F_{11}([hkl], \theta)}, \quad (10)$$

$$G_{[hkl],\theta} = \frac{1}{S'_{44}} = -\frac{1}{S_{44} + A{\cdot}F_{44}([hkl], \theta)}. \quad (11)$$

These equations show that Poisson's ratio and shear modulus depend not only on $[hkl]$ but also on θ. Therefore, a method different from the elastic representative surface should be used to visualize their direction dependency. We adapt the stereographic projection plots in crystallography to show the anisotropy of the two direction-dependent material parameters, $\nu_{[hkl],\theta}$ and $G_{[hkl],\theta}$ [64]. Fig. 3(d) shows examples of stereographic projections of shear modulus and Poisson's ratio, which depict how the shear modulus and Poisson's ratio change as both the loading direction $[hkl]$ and angle θ vary. For instance, as the loading direction $[hkl]$ changes from [001] to [111], the dependency of $G_{[hkl],\theta}$ on θ gradually decreases and finally becomes θ-independent. In contrast, the Poisson's ratio is θ -independent for both the [001] and [111] directions but shows a two-fold symmetry for other loading directions.

In addition to a full two direction-dependent picture, the average values of $\nu_{[hkl],\theta}$ and $G_{[hkl],\theta}$ for a certain direction $[hkl]$ are also desired in many scenarios. These average values can be calculated by integrating over the angle θ as, $\overline{\nu}_{[hkl]} = \frac{1}{2\pi}\int_0^{2\pi}\nu_{[hkl],\theta}d\theta$ and $\overline{G}_{[hkl],\theta} = \frac{1}{2\pi}\int_0^{2\pi}G_{[hkl],\theta}d\theta$, which gives,

$$\overline{\nu}_{[hkl]} = E_{[hkl]}\left\{\frac{\nu 12}{E11} - \frac{A}{k^2+l^2}\left[k^2l^2 + h^2\left(k^4 + k^2l^2 + l^4\right)\right]\right\}, \quad (12)$$

$$1/\overline{G}_{[kl]} = 1/G_{12} + \frac{A}{2\left(k^2+l^2\right)^2}\left[\left(k^2+l^2\right)^4 + \left(h^2k^2 + l^2\right)^2 + \left(k^2 + h^2l^2\right)^2\right]. \quad (13)$$

These averaged parameters only depend on the loading direction $[hkl]$ and can thus be shown in the elastic representative surfaces like Young's modulus.

2.4. Wave propagation calculation

The direction-dependent wave propagation properties are obtained by calculating the dispersion relations based on primitive unit cells in COMSOL Multiphysics. The primitive unit cells and the corresponding irreducible Brillouin zones for HSFs with different lattice structures are summarized in Fig. S2 [65]. The Bloch-Floquet periodic boundary condition is implemented and the eigenfrequency sweep is performed along the edges of the first irreducible Brillouin zone. In the simulation, tetrahedra elements are used and the mesh sensitivity is verified. The dispersion relations are obtained numerically and verified by comparing them with the frequency-domain transmission simulations.

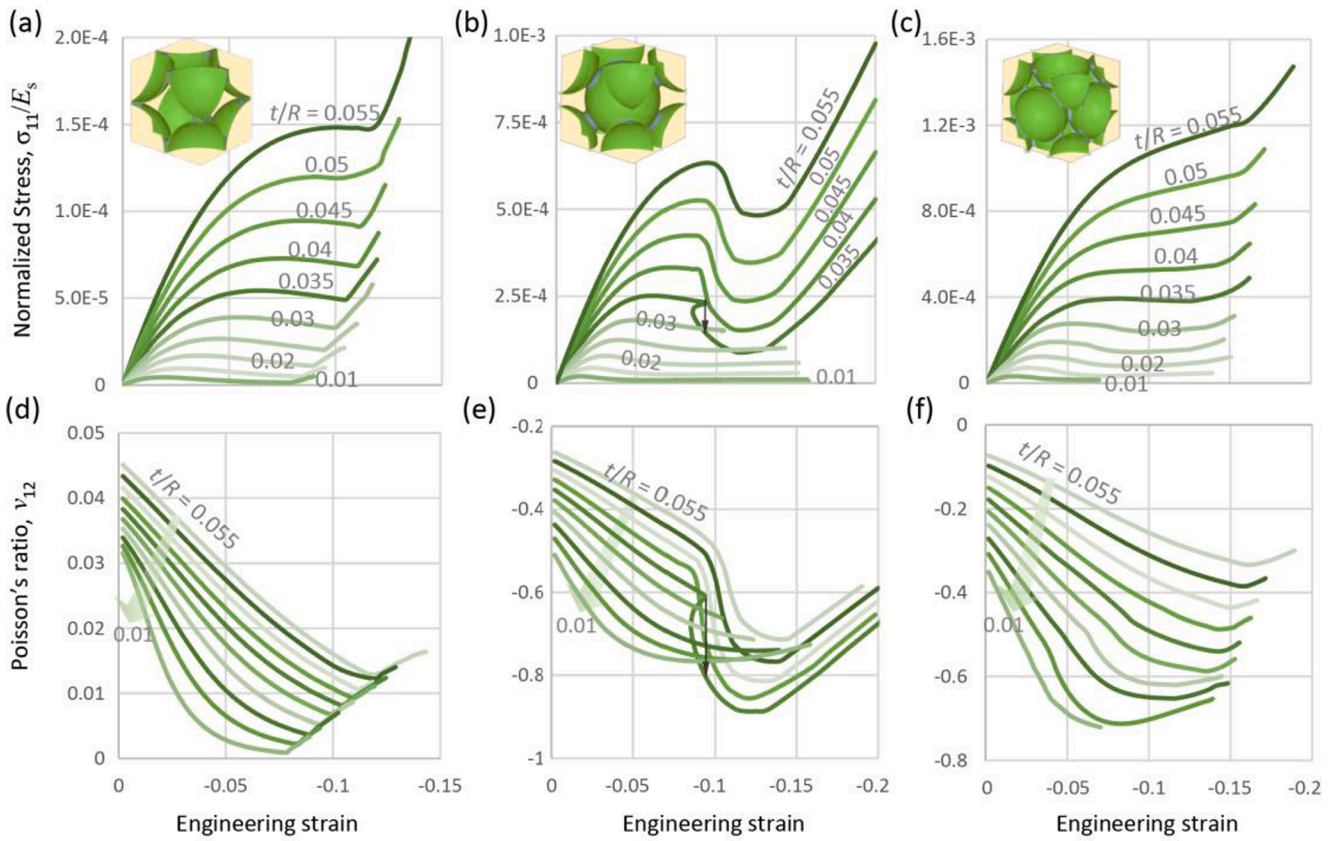

Fig. 4. (a-c) Stress–strain diagram and (d-f) Poisson's ratio-strain diagram of HSFs arranged in SC, BCC, and FCC lattices. $t/R = 0.01$–0.055, $r_b/R = 0.2$, $h/R = 0.02$, $E_b/E_s = 0.04$. The subscripts 1 and 2 of σ_{11} and ν_{12} refer to the [1 0 0] and [0 1 0] directions, respectively.

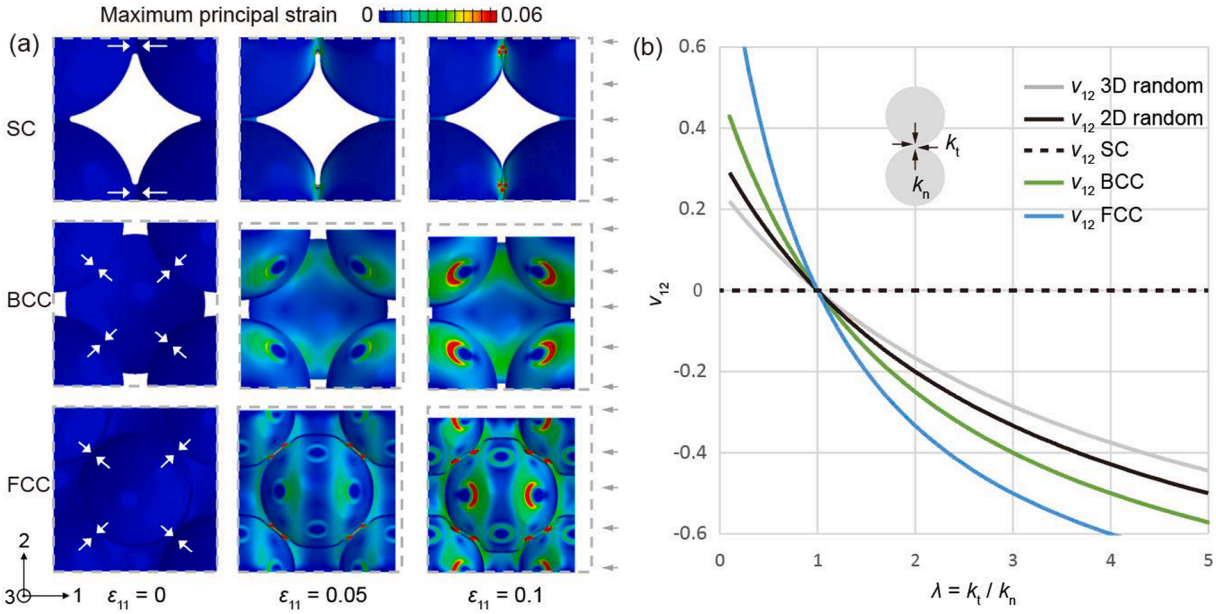

Fig. 5. The auxetic behavior of HSFs. (a) Deformation of HSFs at compressive engineering strain of 0, 0.05, and 0.1. The white arrows mark the directions of recession. $t/R = 0.03$, $r_b/R = 0.2$, $E_b/E_s = 0.04$. (b) Poisson's ratio vs contact stiffness ratio ($\lambda = k_t/k_n$) for spherical shells with different arrangements.

3. Results and discussion

3.1. The elastic constants of HSFs loaded in [1 0 0] direction

We start by investigating the mechanical properties of HSFs under compression. Fig. 4(a-c) summarizes the normalized stress–strain equilibrium paths of HSFs with SC, BCC, and FCC lattices when compressed in the [1 0 0] direction. It is shown that the HSFs with SC and BCC lattices present the typical compressive response of cellular materials, which are featured by three stages – the linear elastic regime, the stable

deformation plateau, and the post-contact strain hardening regime [7]. Such a three-stage behavior renders the HSF material an impressive energy absorption capability. Notably, some of the BCC HSFs exhibit negative incremental stiffness due to the snap-through behavior [Fig. 4 (b)]. More impressively, snap-back is observed in the BCC HSF with $t/R \sim 0.035$, which theoretically leads to an incremental stiffness approaching negative infinity under displacement-controlled loading (marked by black arrows) [33]. This remarkable behavior results from a symmetric to asymmetric deformation pattern change induced by snap-through instability. Detailed discussion on the negative material indices of HSF can be found in [33].

Fig. 4(d–f) summarizes the Poisson's ratio of HSF under uniaxial compression in the [1 0 0] direction. HSF with SC lattice possesses a near-zero (>0) Poisson's ratio. By contrast, the Poisson's ratios of the BCC and FCC lattices are negative and vary in the range of −0.9 to −0.1. Note that different from most auxetic behavior that depends on chiral, reentrant, or rotation mechanisms [7,37,38,66], the auxetic behavior of HSF is based on an "indentation" mechanism as depicted in Fig. 5(a). More specifically, the hollow spheres recess in the center-to-center directions between adjacent spheres. As a result of this deformation mode, HSF with SC lattice exhibits a Poisson's ratio approaching zero, while BCC and FCC lattices exhibit negative Poisson's ratios. This indentation mechanism can be combined with snap-through instability to induce a rapid change of volume, which has been harnessed in actuation devices [33,51].

We further note that the "indentation" mechanism is conditional. It requires the normal contact stiffness (k_n) between adjacent hollow spheres to be smaller than the shear stiffness (k_t) [Fig. 5(b)]. Otherwise, the deformation is shear-dominated instead of indentation-dominated. It has been shown previously that in a randomly packed three-dimensional (3D) granular system, the Poisson's ratio can be calculated by

$$\nu_{3D} = (1-\lambda)/(4+\lambda), \tag{14}$$

where $\lambda = k_t/k_n$ is the shear to normal stiffness ratio [67]; while for 2D random systems, the equation becomes

$$\nu_{2D} = (1-\lambda)/(3+\lambda). \tag{15}$$

Because of the similarity between the granular system and the HSF, these formulas also apply to the randomly packed HSFs. By micro-mechanical analysis, we further show that the Poisson's ratio of BCC and FCC lattices can be derived as

$$\nu_{BCC} = (1-\lambda)/(2+\lambda) \tag{16}$$

and

$$\nu_{FCC} = (1-\lambda)/(1+\lambda). \tag{17}$$

These dependencies of Poisson's ratio on λ for differently packed HSFs are summarized in Fig. 5(b). A comparison of these curves reveals that (1) the condition $\lambda > 1$ is essential to acquire negative Poisson's ratio, which is independent of the packing pattern; (2) arranging HSFs periodically increases the achievable range of Poisson's ratio, which can either limit the Poisson's ratio close to zero or increase the magnitude of the negative Poisson's ratio.

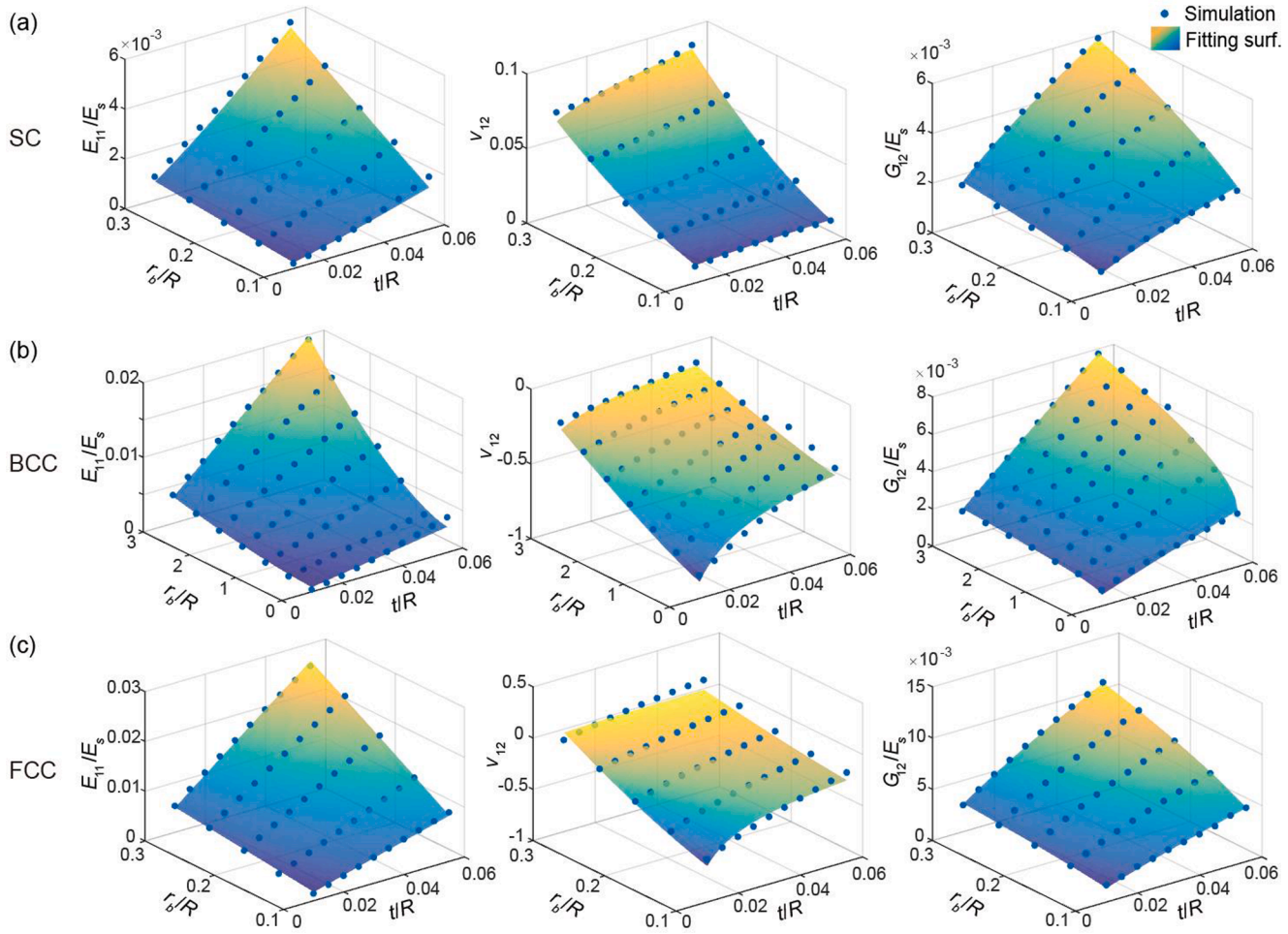

Fig. 6. Comparison between the simulated elastic constants and the results predicted by the general scaling formula for (a) SC, (b) BCC, and (c) FCC packed HSFs.

Table 1

The general scaling formulas to predict the elastic constants of HSFs $P_{eff} = a\left(\frac{t}{R}\right)^{b}\left[\left(\frac{r_b}{R}\right)^{c} + d\right]$

P_{eff}	SC			BCC			FCC		
	E_{11}/E_s	ν_{12}	G_{12}/E_s	E_{11}/E_s	ν_{12}	G_{12}/E_s	E_{11}/E_s	ν_{12}	G_{12}/E_s
a	0.5651	1.1289	0.1307	1.926	0.02294	0.1397	1.292	0.2405	0.2644
b	1.158	0.1778	0.7279	1.010	−0.4136	0.9499	0.9778	−0.6674	0.7955
c	1.058	1.897	0.3206	1.527	1.172	0.5154	0.7965	1.619	0.3259
d	0	0.00786	−0.3088	0.03322	−5.764	0.3387	−0.03598	−0.1491	−0.2734
R^2	0.9912	0.9943	0.9970	0.9935	0.9659	0.9945	0.9975	0.9351	0.9985

3.2. General scaling relationship of the elastic properties

Tailorable mechanical property is one important advantage of lattice materials compared to random cellular materials. As already shown above, the stress–strain curve and the Poisson's ratio of HSFs can be controlled by adjusting the relative thickness of the spherical shells. To further guide the design of the HSFs, parametric numerical simulations are performed to obtain quantitative design formulas. Specifically, the geometric parameters are varied in the simulation with t/R = 0.01–0.055 and r_b/R = 0.1–0.3. The calculated Young's modulus, shear modulus, and Poisson's ratio are plotted as functions of the geometric dimensions in Fig. 6. Based on the numerical results, it is found that all three normalized elastic constants of HSFs can be described by the following scaling relationship,

$$P_{eff} = a\left(\frac{t}{R}\right)^{b}\left[\left(\frac{r_b}{R}\right)^{c} + d\right], \tag{18}$$

where P_{eff} is the normalized material property, i.e., E_{11}/E_s, G_{12}/E_s, or ν_{12}. a, b, c, and d are fitting parameters. By using the trust-region algorithm with the objective function to maximize the coefficient of determination (R^2), the simulation results are fitted to Eq. (18) [68], with $R^2 = 1$ representing a perfect fitting. Table 1 summarizes the fitting parameters together with the R^2 value calculated by a customized Matlab program. A comparison of the numerical data to the fitting surfaces is shown in Fig. 6. Impressively, the fitting surfaces based on Eq. (18) capture the simulation data points very well, which is a qualitative reflection of $R^2 \approx 1$, as summarized in Table 1. As such, the scaling equations provide a rapid and easy way to predict the elastic constants of periodic HSF.

We further highlight that the scaling parameter b of the normalized stiffness (i.e., $E_{11}/E_s \sim (t/R)^b$) for all the investigated HSFs is close to 1. Specifically, $b = 1.16$ for the SC lattice, $b = 1.01$ for the BCC lattice, and $b = 0.98$ for the FCC lattice, suggesting that the normalized stiffness of all three architected HSFs scales linearly with t/R. Recalling the result in Section 2.1 that relative density $\rho/\rho_s \propto t/R$, we have $E_{11}/E_s \propto \rho/\rho_s$. This linear scaling relationship is characteristic of compression/stretching-

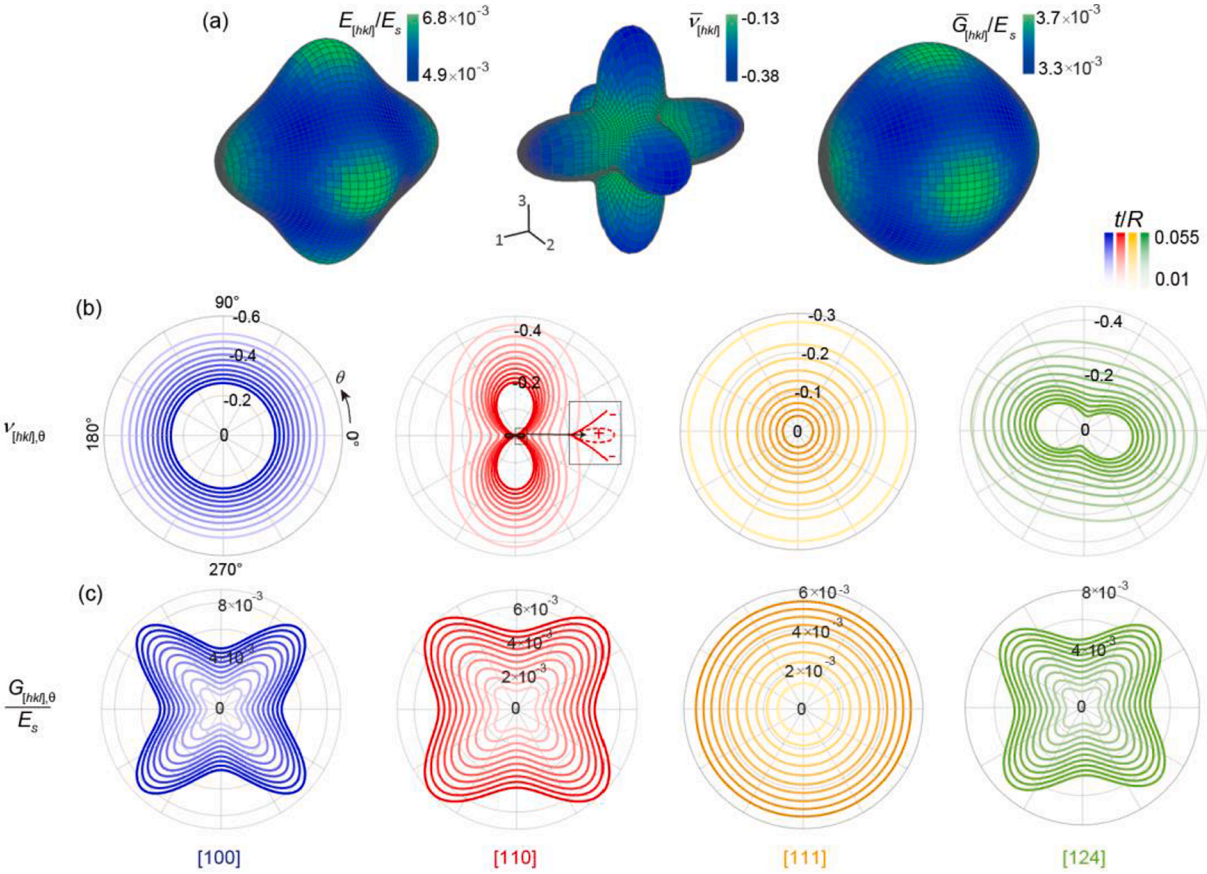

Fig. 7. Direction-dependent mechanical behavior of BCC packed HSFs lattice. (a) Elastic representative surface of normalized $E_{[hkl]}$, $\bar{\nu}_{[hkl]}$, and $\bar{G}_{[hkl]}$ with $t/R = 0.03$. (b) Polar distribution of Poisson's ratio and (c) shear modulus in the [1 0 0], [1 1 0], [1 1 1], and [1 2 4] directions. The gradient color in (b,c) presents t/R varying from 0.01 to 0.055. The dashed line highlights regions with positive Poisson's ratio. Here, $r_b/R = 0.2$, $h/R = 0.02$, and $E_b/E_s = 0.04$.

dominated deformation [69]; thereby, the deformation of HSFs at small deformation is compression-dominated, regardless of the thin curvy shape of the hollow spheres. A comparison of HSFs with other ultra-stiff lattices reveals that the HSFs have a similar specific stiffness to the octet truss [1], a structure previously shown to be ultra- stiff and strong [10,11]. This result suggests the potential of using HSFs as candidates for lightweight, stiff, and strong micro-lattices, in addition to its multi-functionality summarized in Fig. 1. It should be noted though, that experimental results of 3D printed periodic spherical foams show a scaling factor b = 1.56, this may be related to either manufacturing defects or the holes introduced in the hollow spheres (to enable 3D printing) [70].

In addition to geometric parameters, the effect of material constituents on the elastic properties of HSF is also investigated. The mechanical properties of the HSF are strongly affected by the stiffness ratio between the binder and the shell, E_b/E_s. The calculated design map of elastic constants of HSFs with a variation of E_b/E_s in the range of 0.01 to 25 is shown in Fig. S3. Notably, varying E_b/E_s has a similar effect as varying r_b/R, meaning that making the binder softer has a similar effect as making the binder smaller.

3.3. Direction-dependent mechanical properties

With the elastic constants E_{11}, ν_{12}, and G_{12} predicted accurately by the general scaling formula, we further seek to determine the anisotropic mechanical properties of HSFs. As discussed in Section 2.3, effective modulus only depends on the loading direction [*hkl*], which can be written as $E_{[hkl]}$ and visualized using the elastic representative surface. Combing FEM simulation with Eqs. (6)–(13) allow us to plot the direction-dependent elastic properties of BCC HSF (t/R = 0.03, r_b/R = 0.2, h/R = 0.02) in Fig. 7(a), where the direction-dependent properties of elastic modulus, average shear stiffness $\overline{G}_{[hkl]}$, and average Poisson's ratio $\overline{\nu}_{[hkl]}$ (averaged over θ) are summarized. It is found that the BCC HSFs have the maximum $E_{[hkl]}$, maximum $\overline{G}_{[hkl]}$, but minimum $\overline{\nu}_{[hkl]}$ in the [1 0 0] direction. In contrast, $E_{[hkl]}$ and $\overline{G}_{[hkl]}$ acquire their minimum values in the [1 1 1] direction. Importantly, for all loading directions, $\overline{\nu}_{[hkl]}$ varies in the range of −0.38 to −0.13, suggesting that the BCC HSF can exhibit omnidirectional auxetic behavior.

Furthermore, Poisson's ratio $\nu_{[hkl],\theta}$ and shear modulus $G_{[hkl],\theta}$ depend on two directions, with θ denoting the second direction. To depict $\nu_{[hkl],\theta}$ and $G_{[hkl],\theta}$, we fix [*hkl*] in selected orientations ([1 0 0], [1 1 0], [1 1 1], and [1 2 4]) and then plot the variation of $\nu_{[hkl],\theta}$ and $G_{[hkl],\theta}/E_s$ as θ changes from 0 to π. The results of BCC HSF are shown in Fig. 7(b,c), where the relative thickness t/R varies from 0.01 to 0.055. Interestingly, in the [1 0 0] and [1 1 1] directions, the polar plots of Poisson's ratio are circles, meaning that the HSFs contract equally in all lateral directions when compressed in these directions. The simulated isotropic property in these planes may not be a direct result of the structural symmetry but due to affine deformation, as the BCC lattice has only a three-fold symmetry in the {1 1 1} plane. Moreover, the polar plots of $\nu_{[hkl],\theta}$ show peanut shape in the [1 1 0] direction, exhibiting a strong direction dependency. Such peanut shapes are common for general [*hkl*] directions as shown in Fig. 3(d). Interestingly, the BCC HSF can exhibit a negative Poisson's ratio in certain directions but exhibit a positive Poisson's ratio in others. For instance, the BCC lattice with t/R = 0.05 exhibits positive Poisson's ratio near $\theta = 0°$ (marked by the dashed curve in [1 1 0] plot of Fig. 7(b)). Such a characteristic feature could enable functional devices like auxetic effect-based switchers for light/flow control.

Compared to the general two-fold symmetry of Poisson's ratio in the θ plane, the shear modulus exhibits a four-fold angular symmetry. As shown in Fig. 7(c), the angular dependency of $G_{[hkl],\theta}$ on θ is most significant in the [1 0 0] direction, while isotropic behavior is observed in the [1 1 1] direction.

In addition to shell thickness, the effect of binder radius on the anisotropic properties is further plotted in Fig. 8. Again, the effect of increasing binder radius [Fig. 8(a,b)] has a similar effect as increasing the shell thickness [Fig. 7(b,c)]: they both reduce the Poisson's ratio and increase the shear modulus. Importantly, the effective properties of HSFs depend strongly on both [*hkl*] and θ. So, given a specific HSF, we can obtain different elastic properties by simply changing the loading direction or varying the orientation of the material. For example, under compression in [1 1 0] direction, if we change the material orientation (θ direction) from 0° to 90°, the Poisson's ratio markedly changes from +0.05 to –0.12.

The direction-dependent performances reported so far focus on HSFs arranged in a BCC lattice, Fig. S4 and Fig. S5 further summarize the direction-dependent properties of FCC and SC packed HSFs. The FCC lattice presents anisotropic properties similar to that of the BCC lattice but with a less significant anisotropy. By contrast, the SC lattice shows a different anisotropic profile. Specifically, the SC lattice exhibits the

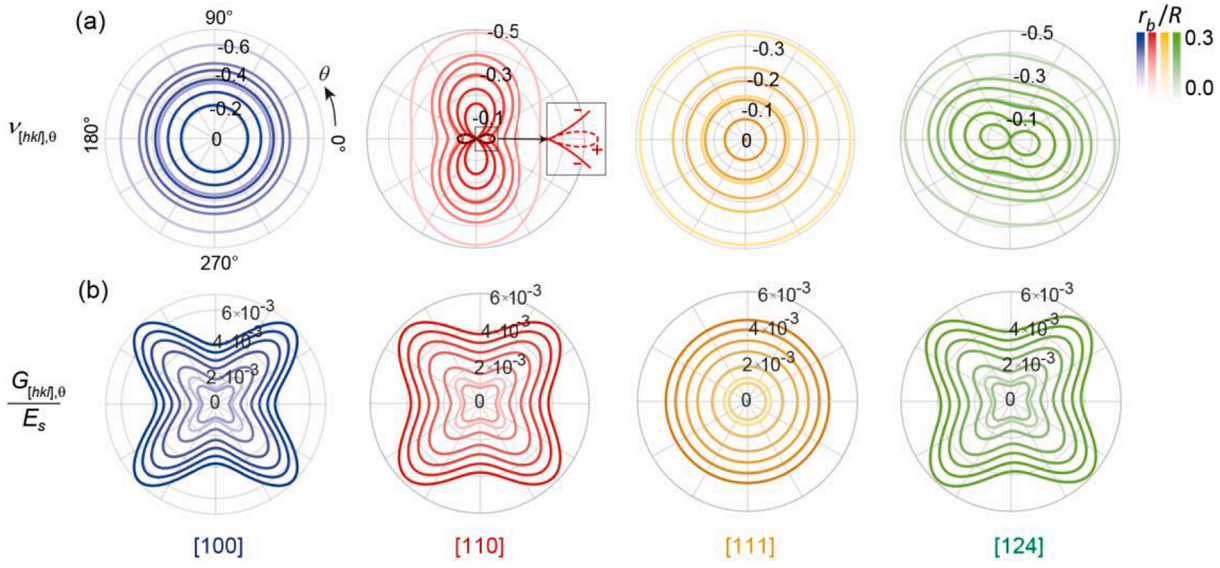

Fig. 8. Effect of varying binder radius on the direction-dependent properties of BCC packed HSFs. Polar plots of (a) Poisson's ratio and (b) shear modulus with [*hkl*] selected as [1 0 0], [1 1 0], [1 1 1], and [1 2 4]. r_b/R = 0.2, h/R = 0.02, and E_b/E_s = 0.04. The gradient color presents r_b/R varying from 0 to 0.3. The dashed curve marks a positive Poisson's ratio.

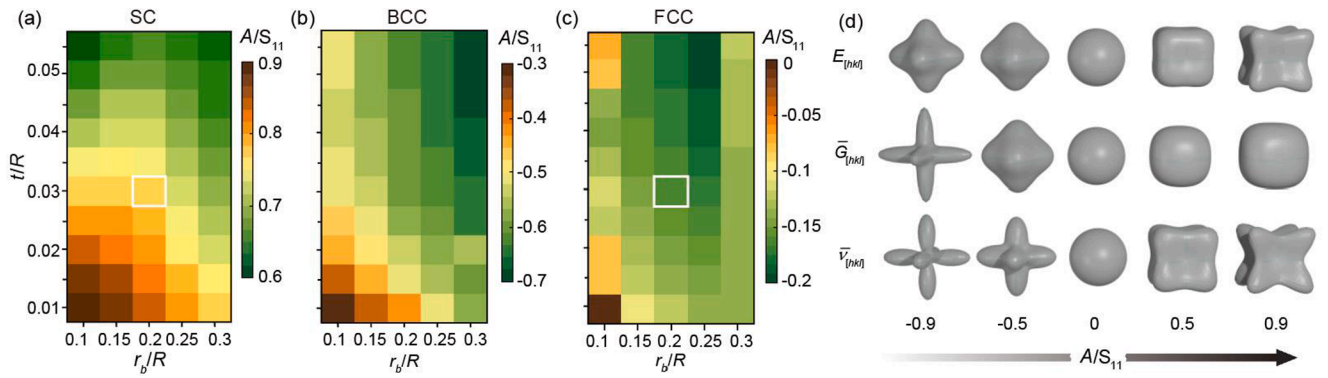

Fig. 9. (a-c) Anisotropic ratio of SC, BCC, and FCC packed HSFs with varying geometric parameters. The white squares mark the structural designs whose anisotropic properties are further analyzed in Fig. 10. (d) Design map that depicts mechanical anisotropy based on parameter A/S_{11}.

minimum $E_{[hkl]}$, minimum $\overline{G}_{[hkl]}$, and maximum $\overline{\nu}_{[hkl]}$ in the [100] direction, contrary to the BCC and FCC lattices. In addition, for the investigated geometric sizes, all SC lattices always exhibit a small positive Poisson's ratio when loaded in the [100] direction.

In summary, HSFs packed in SC lattice show the most significant direction-dependent properties, which is advantageous for applications like direction-sensitive force sensors and Poisson's ratio switchers. In contrast, the FCC HSF can be designed for quasi-isotropic elastic properties, the highest stiffness of HSFs, and omnidirectional negative Poisson's ratio. The elastic anisotropy of BCC HSF is intermediate between SC and FCC. Besides the geometric features, the constituent properties can be further adjusted to achieve a substantial design space of direction-dependent elastic profiles [Fig. S3(d–e)].

3.4. Quantification of the anisotropic profiles

The direction-dependent properties have been visualized qualitatively in elastic representative surfaces and stereographic projection-based polar plots; we next seek a quantitative description of mechanical anisotropy. The general relationship in Eq. (5), $S'_{ij} = S_{ij} + A \cdot F_{ij}([hkl], \theta)$, gives a mathematical description of the direction-dependent elastic properties of cubic materials as functions of $[hkl]$ and θ. As S_{ij} is a constant and the function $F_{ij}([hkl], \theta)$ is solely defined by the lattice symmetry, so, the greater the value of A, the greater the mechanical anisotropy. As such, the normalized A value, A/S_{11}, can be used as a quantitative metric to describe the mechanical anisotropy of cubic materials. Fig. 9(a–c) summarize the dependency of A/S_{11} on shell thickness and binder size through simulation. Impressively, HSFs with different lattice types exhibit different ranges of the anisotropic parameter, which together, covers a wide range of A/S_{11} values in the range of -0.7 to 0.9. Specifically, SC packed HSFs with smaller binder sizes and thinner shells exhibit stronger anisotropy ($A/S_{11} = 0.9$). In contrast, BCC lattices with larger binder sizes and thicker shells exhibit greater anisotropy ($A/S_{11} = -0.7$). The FCC packed HSFs, in contrast, can be designed for quasi-isotropic properties. For instance, the FCC packed HSF shows $A/S_{11} = 0.004$ with $r_b/R = 0.2$ and $t/R = 0.01$, which is close to isotropic ($A/S_{11} = 0$). The wide range of anisotropic elastic profiles are visualized in Fig. 9(d) based on parameter A/S_{11}. Note that this anisotropic map is true for all cubic materials (not limited to the HSFs of this study, but also truss-based structures, diamond lattices, etc). For designs in Fig. 9(a-c), the anisotropy level of the three elastic constants can be indexed using this map.

In addition to geometric parameters, the anisotropic parameter also depends significantly on E_b/E_s (Fig. S6). This is a highly desired feature for engineering smart and adaptive lattice materials because the stiffness contrast E_b/E_s can be actively controlled by adjusting the binder properties using heat or light. For instance, if the binders are fabricated by

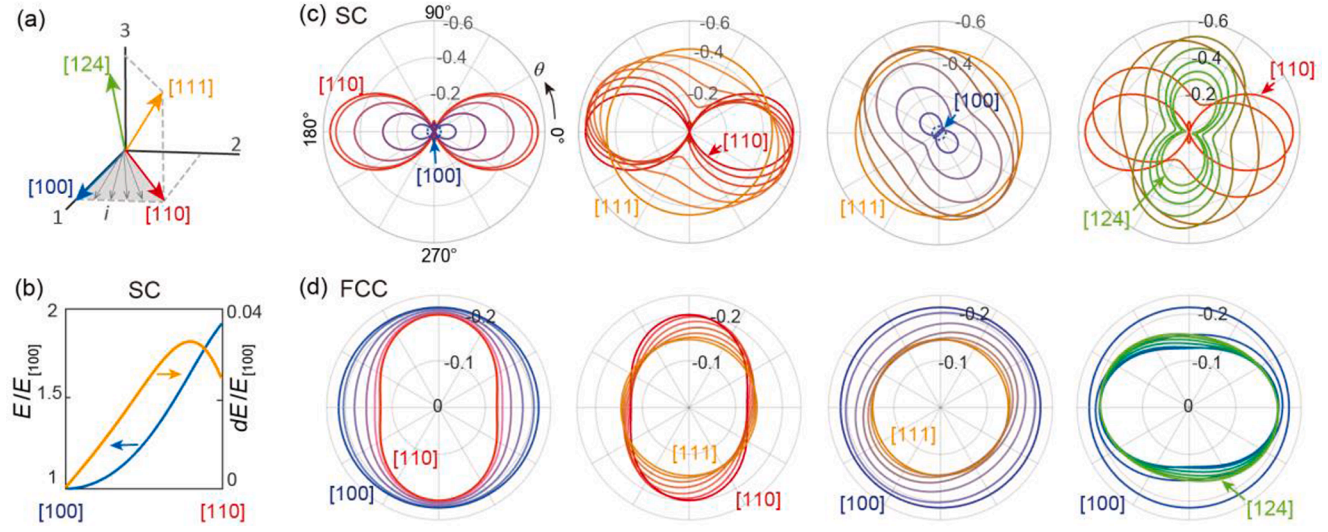

Fig. 10. Evolution of material property as the load direction varies. (a) Definition of the [100], [110], [111], and [124] loading directions. (b) Variation of normalized modulus $E/E_{[100]}$ as load direction changes. $dE/E_{[100]}$ is the change of normalized effective modulus per degree. (c-d) Variation of Poisson's ratio profile as the load direction changes between [100], [110], [111], and [124] directions. The solid and dashed curves represent negative and positive Poisson's ratios, respectively.

temperature-sensitive shape memory polymers, HSFs with anisotropy programmable by temperature can be readily produced.

3.5. Evolution of elastic properties as functions of the loading direction

The direction-dependent material properties of HSFs also enable the active control of mechanical performance by simply rotating the material (for example, if we shape the structured material into a sphere). To show the evolution of elastic properties with respect to the change of the loading direction, the SC packed HSF, which exhibits a strong direction dependency, is used for demonstration. Specifically, we plot the normalized Young's modulus of SC packed HSF as the loading direction changes from the [1 0 0] to the [1 1 0] direction [Fig. 10(a)]. In this range of direction variation, the normalized stiffness increases impressively by over 90%, corresponding to a change in normalized effective stiffness per degree ($dE/E_{[100]}$) of 0.04 [Fig. 10(b)], which means 2.5 degrees of angle change can impressively give rise to 10% modulus variation. For a typical HSF foam material made of aluminum, $E_{[100]} \approx 20$ MPa, the corresponding change of stiffness per degree is estimated as 0.8 MPa. Combining such a significant change in stiffness with deformation-sensitive electrical materials [26], the SC packed HSF can be used to develop sensors that detect the change of loading direction.

More systematic evolutions of Poisson's ratio as the loading direction changes between [1 0 0], [1 1 0], [1 1 1], and [1 2 4] directions are depicted in Fig. 10(c) and (d) for SC and FCC HSFs, respectively. The geometric parameters of these two HSFs are marked by white rectangles in Fig. 9(a) and (c). Clearly, the SC HSF presents a strong direction dependency, whose Poisson's ratio can vary from positive to negative or vary from peanut shape to circular shape depending on the loading direction. Differently, the Poisson's ratio of the FCC HSF presents a relatively weak direction dependency, which maintains auxetic behavior for all loading directions. The wide range of direction-dependent profiles demonstrated here opens the avenue to design anisotropic property-critical materials for tissue growth direction control, bone scaffolds, and metamaterials.

3.6. Direction-dependent wave propagation and phononic band structure

Having demonstrated the anisotropic elastic properties of HSFs, we next show their direction-dependent wave propagation performance. Specifically, we calculate the wave propagation characteristic of HSFs for incident waves from different directions, which is presented in the band diagram (also known as the dispersion relation). Fig. 11 (a) and (b) show the calculated band diagram of two designs, one with $r_b = 2.0$, $h = 0.2$, $t = 1.0$ and one with $r_b = 0.2$, $h = 0.2$, $t = 1.0$ (R is fixed as 10). The shaded regions mark the complete band gaps, in which frequency range, elastic waves of arbitrary incident direction cannot propagate through. Fig. 11(c) further shows the evolution of band gaps as a function of the cell wall thickness t for three groups of parameters: the red color

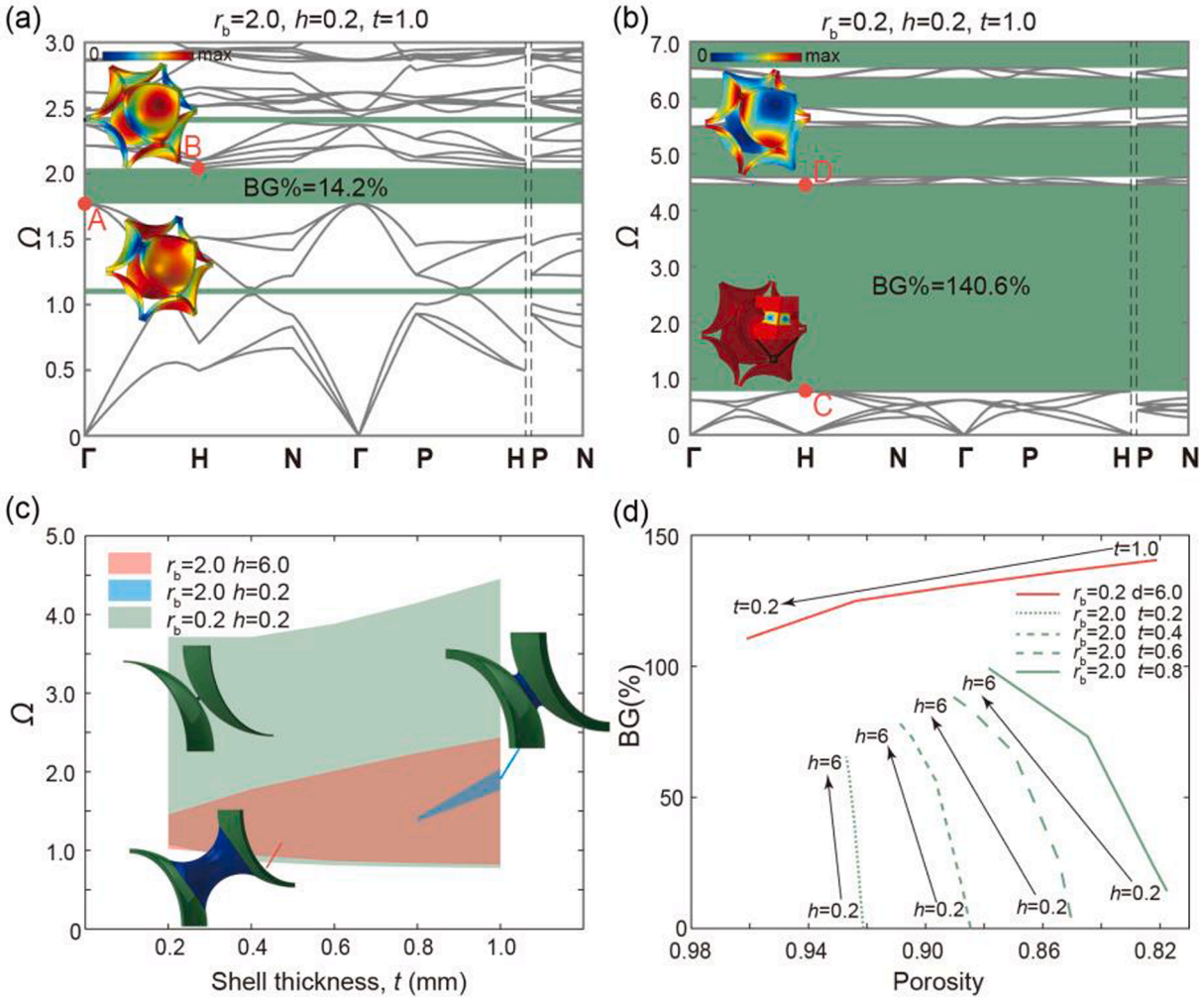

Fig. 11. (a, b) Dispersion relation and Bloch modes of the BCC packed HSF with (a) $r_b = 2$, $h = 0.2$, and $t = 1.0$ and (b) $r_b = 0.2$, $h = 0.2$, and $t = 1.0$. R is fixed as 10. (c) Evolution of the band gaps as functions of the shell thickness. (d) Band gaps width vs porosity with varying shell thickness (red line) and binder height (green lines). (For interpretation of the references to color in this figure legend, the reader is referred to the web version of this article.)

represents HSFs with fixed $r_b = 2.0$, $h = 6.0$, the blue color represents $r_b = 2.0$, $h = 0.2$, and green color represents $r_b = 0.2$, $h = 0.2$. Complete band gaps exist for a wide range of geometric parameters and become extremely wide for small or long binder connections. Increasing h, decreasing r_b, and making the shells thicker all make the band gap wider. These variations of geometric parameters widen the bandgap by two mechanisms: (1) decreasing the equivalent stiffness of the binder and (2) increasing the equivalent stiffness of the shell, which magnifies the stiffness contrast between the shell and the binder.

To further understand the formation mechanism of the observed wide band gaps, we analyze the eigenmodes on the upper and lower edges of the bandgap in Fig. 11 (a) and (b). Both these two designs exhibit maximum bandgaps between the 6^{th} and 7^{th} modes with relative gap widths (BG%) of 14.2% and 140.6%, respectively. While the localized Bloch mode and the narrow bandgap in Fig. 11(a) indicate that the bandgap is produced by local resonance, the peaks and valleys in the edges of the bandgap suggest that the bandgap is not formed purely by local resonance – Bragg scattering might also be a reason. As for the second case in Fig. 11(b), the non-localized deformation of Bloch mode (large displacement is observed in the entire structure), non-flat band edge, and the normalized frequency $\Omega \approx 1$ provide evidence that the lower edge of the bandgap is produced by Bragg scattering. The localized deformation and the flat band edge on the upper edge, however, suggested that the formation mechanism is also related to local resonance. Based on these two examples of different geometric parameters, the wide band gap in HSFs results from the coupling between Brag wave scattering and local resonances.

One advantage of HSFs compared to many other phononic crystals is their high porosity and low density. To highlight HSFs as a low-density, wide band gap phononic crystal, we plot the band gap width as functions of porosity in Fig. 11(c). The plot reveals that HSF with a porosity of 0.82 exhibits a BG% of 140.6%. In particular, the porosity of HSF can be controlled by the thickness of the sphere t, the binder radius, r_b, and/or binder height, h. The effects of these parameters on porosity and BG% are summarized in Fig. 11(d). Specifically, the red line describes the dependency of BG% on porosity variation induced by shell thickness in the range of $t = 0.2$–1.0 ($r_b = 0.2$, $h = 6.0$). When the porosity is tailored by thickness, BG% increases slowly at decreased porosity and the variation of BG% is modest. In contrast, when porosity is tailored by changing the binder height, h, BG% depends strongly on the porosity, as shown by the large slope of the green lines (plotted with fixed $r_b = 2.0$ and varying $h = 0.2$–6.0) in Fig. 11(d). The important knowledge we learned based on the above parametric analysis is: first, the band gap width of HSFs can either increase or decrease as a function of porosity, which depends on the tailored design parameter; second, high porosity and wide bandgap can be achieved simultaneously in HSFs.

Compared to HSFs packed in BCC lattice, HSFs with SC and FCC packings possess a similar wave propagation characteristic. The band diagrams of the HSF arranged in SC and FCC lattices are shown in Fig. S7. The geometric parameters are set to be the same as BCC HSF shown in Fig. 11(b). Compared to the BCC HSF, the maximum band gaps are also between 6^{th} and 7^{th} modes and the band gap width is also around 140%, suggesting a similar band gap formation mechanism. Thus, the parametric analysis discussed above for BCC HSFs can be applied to HSFs arranged in SC and FCC lattices as well.

Finally, we note that although HSF provides a promising design motif for achieving multiple desired functions, some limitations should be noted. First, its manufacturing is challenging, as the enclosed hollow cells cannot be directly produced by 3D printing. Second, the enclosed hollow spheres may form residual stresses if the HSF experiences a temperature change that affects the pressure inside the spheres. Third, reducing manufacturing defects is also important to acquire the predicted properties. In further studies, developing new fabrication techniques that enable direct production of HSF with minimized defects is highly desired.

4. Conclusions

We have showed a general approach to study the direction-dependent static mechanical properties and the dynamic wave propagation properties of lattice materials by combining numerical simulations and theoretical analysis. Explicit formulas are derived to present the elastic constants of cubic materials in arbitrary loading directions. Stereographic projections are demonstrated as a feasible way to present the anisotropic profiles of shear modulus and Poisson's ratio. The band diagram further provides a depiction of the direction-dependent wave propagation properties of lattice materials. The developed method can be applied to cubic symmetric materials and also extended to materials with other symmetries.

Using the developed approach, the anisotropic mechanical properties of HSFs are studied. The design space of the elastic constants of HSFs is formulated analytically by a general scaling relationship. These scaling formulas enable the efficient design of HSFs with desired elastic properties and anisotropic profiles. HSFs with different anisotropic profiles, omnidirectional negative Poisson's ratio, and wide band gap (BG% = 150%) at high porosity (0.85) are obtained by tailoring the geometric parameters. The developed method also enables the visualization of how elastic properties vary continuously as the loading direction changes, opening avenues to design direction-sensitive materials and sensors.

The direction-dependent properties of HSF can be combined with previously demonstrated functionalities of HSFs. We hope the methods and results reported here on HSFs can inform the design of smart porous and composite materials with extreme lightweight, direction-sensitivity, reconfigurability, programmability, and multifunctionality.

CRediT authorship contribution statement

Zian Jia: Conceptualization, Formal analysis, Investigation, Methodology, Writing – original draft, Writing – review & editing. **Fan Liu:** Formal analysis, Investigation, Methodology, Writing – original draft, Writing – review & editing. **Ling Li:** Funding acquisition, Supervision, Writing – review & editing. **Lifeng Wang:** Conceptualization, Funding acquisition, Supervision, Writing – review & editing.

Declaration of Competing Interest

The authors declare that they have no known competing financial interests or personal relationships that could have appeared to influence the work reported in this paper.

Acknowledgment

The authors gratefully acknowledge the financial support from the National Science Foundation (CMMI-1462270) and the Air Force Office of Scientific Research (FA9550-20-1-0161). Z. J. also thanks Dr. Yanyu Chen at the University of Louisville for beneficial discussions.

Appendix A. Supplementary material

Supplementary data to this article can be found online at https://doi.org/10.1016/j.compstruct.2022.115540.

References

[1] Jia Z, Liu F, Jiang X, Wang L. Engineering lattice metamaterials for extreme property, programmability, and multifunctionality. J Appl Phys 2020;127(15):150901. https://doi.org/10.1063/5.0004724.
[2] Valdevit L, Jacobsen AJ, Greer JR, Carter WB, Pollock TM. Protocols for the optimal design of multi-functional cellular structures: from hypersonics to micro-architected materials. J Am Ceram Soc 2011;94:s15–34.
[3] Lincoln RL, Scarpa F, Ting VP, Trask RS. Multifunctional composites: A metamaterial perspective. Multifunct Mater 2019;2(4):043001. https://doi.org/10.1088/2399-7532/ab5242.

[4] Zhang Z, Lei H, Yang H, Chen M, Wang C, Yang H, et al. Novel multifunctional lattice composite structures with superior load-bearing capacities and radar absorption characteristics. Compos Sci Technol 2021;216:109064. https://doi.org/10.1016/j.compscitech.2021.109064.

[5] Puthanveetil S, Liu WC, Riley KS, Arrieta AF, Le Ferrand H. Programmable multistability for 3D printed reinforced multifunctional composites with reversible shape change. Compos Sci Technol 2022;217:109097. https://doi.org/10.1016/j.compscitech.2021.109097.

[6] Zhao W, Liu Z, Yu G, Wu L. A new multifunctional carbon fiber honeycomb sandwich structure with excellent mechanical and thermal performances. Compos Struct 2021;274:114306. https://doi.org/10.1016/j.compstruct.2021.114306.

[7] Gibson LJ, Ashby MF. Cellular solids: structure and properties. Cambridge University Press; 1997.

[8] Ashby M, Evans A, Gibson L, Hutchinson J, Fleck N, Wadley H. Cellular metals, a design guide. Cambridge: Cambridge University, Engineering Department; 1998.

[9] Evans AG, Hutchinson J, Ashby M. Multifunctionality of cellular metal systems. Prog Mater Sci 1998;43:171–221.

[10] Meza LR, Das S, Greer JR. Strong, lightweight, and recoverable three-dimensional ceramic nanolattices. Science 2014;345(6202):1322–6.

[11] Zheng X, Lee H, Weisgraber TH, Shusteff M, DeOtte J, Duoss EB, et al. Ultralight, ultrastiff mechanical metamaterials. Science 2014;344(6190):1373–7.

[12] Jia Z, Yu Y, Wang L. Learning from nature: Use material architecture to break the performance tradeoffs. Mater Des 2019;168:107650. https://doi.org/10.1016/j.matdes.2019.107650.

[13] Ritchie RO. The conflicts between strength and toughness. Nat Mater 2011;10(11):817–22.

[14] Chen Y, Jia Z, Wang L. Hierarchical honeycomb lattice metamaterials with improved thermal resistance and mechanical properties. Compos Struct 2016;152:395–402.

[15] Jia Z, Wang Z, Hwang D, Wang L. Prediction of the effective thermal conductivity of hollow sphere foams. ACS Appl Energy Mater 2018;1(3):1146–57.

[16] Gu GX, Chen C-T, Richmond DJ, Buehler MJ. Bioinspired hierarchical composite design using machine learning: simulation, additive manufacturing, and experiment. Mater Horiz 2018;5(5):939–45.

[17] Wang Q, Jackson JA, Ge Qi, Hopkins JB, Spadaccini CM, Fang NX. Lightweight mechanical metamaterials with tunable negative thermal expansion. Phys Rev Lett 2016;117(17). https://doi.org/10.1103/PhysRevLett.117.175901.

[18] Li Y, Chen Y, Li T, Cao S, Wang L. Hoberman-sphere-inspired lattice metamaterials with tunable negative thermal expansion. Compos Struct 2018;189:586–97.

[19] Hollister SJ. Porous scaffold design for tissue engineering. Nat Mater 2005;4(7):518–24.

[20] Gonella S, To AC, Liu WK. Interplay between phononic bandgaps and piezoelectric microstructures for energy harvesting. J Mech Phys Solids 2009;57(3):621–33.

[21] Sanders WS, Gibson LJ. Mechanics of hollow sphere foams. Mater Sci Eng, A 2003;347(1-2):70–85.

[22] Sanders WS, Gibson LJ. Mechanics of BCC and FCC hollow-sphere foams. Mater Sci Eng, A 2003;352(1-2):150–61.

[23] Zeng HB, Pattofatto S, Zhao H, Girard Y, Fascio V. Impact behaviour of hollow sphere agglomerates with density gradient. Int J Mech Sci 2010;52(5):680–8.

[24] Zhu Y, Liang S, Chen K, Gao X, Chang P, Tian C, et al. Preparation and properties of nanoencapsulated n-octadecane phase change material with organosilica shell for thermal energy storage. Energy Convers Manage 2015;105:908–17.

[25] Cochran JK. Ceramic hollow spheres and their applications. Curr Opin Solid State Mater Sci 1998;3(5):474–9.

[26] Pan L, Chortos A, Yu G, Wang Y, Isaacson S, Allen R, et al. An ultra-sensitive resistive pressure sensor based on hollow-sphere microstructure induced elasticity in conducting polymer film. Nat Commun 2014;5(1). https://doi.org/10.1038/ncomms4002.

[27] Vesenjak M, Duarte I, Baumeister J, Göhler H, Krstulović-Opara L, Ren Z. Bending performance evaluation of aluminium alloy tubes filled with different cellular metal cores. Compos Struct 2020;234:111748. https://doi.org/10.1016/j.compstruct.2019.111748.

[28] Duarte I, Vesenjak M, Krstulović-Opara L, Ren Z. Compressive performance evaluation of APM (Advanced Pore Morphology) foam filled tubes. Compos Struct 2015;134:409–20.

[29] Wang Z, Zhang T, Park BK, Lee WI, Hwang DJ. Minimal contact formation between hollow glass microparticles toward low-density and thermally insulating composite materials. J Mater Sci 2017;52(11):6726–40.

[30] Ashby M, Evans A, Fleck N, Gibson L, Hutchinson J, Wadley H. Metal foams: a design guideButterworth Heinemann. Boston 2000.

[31] Henzie J, Grünwald M, Widmer-Cooper A, Geissler PL, Yang P. Self-assembly of uniform polyhedral silver nanocrystals into densest packings and exotic superlattices. Nat Mater 2012;11:131–7.

[32] Yin J, Retsch M, Thomas EL, Boyce MC. Collective mechanical behavior of multilayer colloidal arrays of hollow nanoparticles. Langmuir 2012;28(13):5580–8.

[33] Jia Z, Wang L. Instability-triggered triply negative mechanical metamaterial. Phys Rev Appl 2019;12(2). https://doi.org/10.1103/PhysRevApplied.12.024040.

[34] Jia Z, Chen Y, Yang H, Wang L. Designing Phononic Crystals with Wide and Robust Band Gaps. Phys Rev Appl 2018;9(4). https://doi.org/10.1103/PhysRevApplied.9.044021.

[35] Wang L, Bertoldi K. Mechanically tunable phononic band gaps in three-dimensional periodic elastomeric structures. Int J Solids Struct 2012;49(19-20):2881–5.

[36] Chen Y, Li T, Scarpa F, Wang L. Lattice metamaterials with mechanically Tunable Poisson's ratio for vibration control. Phys Rev Appl 2017;7(2). https://doi.org/10.1103/PhysRevApplied.7.024012.

[37] Lakes R. Foam structures with a negative Poisson's ratio. Science 1987;235(4792):1038–40.

[38] Bückmann T, Schittny R, Thiel M, Kadic M, Milton GW, Wegener M. On three-dimensional dilational elastic metamaterials. New J Phys 2014;16(3):033032. https://doi.org/10.1088/1367-2630/16/3/033032.

[39] Sigalas MM. Defect states of acoustic waves in a two-dimensional lattice of solid cylinders. J Appl Phys 1998;84(6):3026–30.

[40] Wang P, Casadei F, Shan S, Weaver JC, Bertoldi K. Harnessing buckling to design tunable locally resonant acoustic metamaterials. Phys Rev Lett 2014;113(1). https://doi.org/10.1103/PhysRevLett.113.014301.

[41] Spadoni A, Ruzzene M, Gonella S, Scarpa F. Phononic properties of hexagonal chiral lattices. Wave Motion 2009;46(7):435–50.

[42] Spadoni A, Ruzzene M. Elasto-static micropolar behavior of a chiral auxetic lattice. J Mech Phys Solids 2012;60(1):156–71.

[43] Khelif A, Choujaa A, Benchabane S, Djafari-Rouhani B, Laude V. Guiding and bending of acoustic waves in highly confined phononic crystal waveguides. Appl Phys Lett 2004;84(22):4400–2.

[44] Vasseur JO, Hladky-Hennion A-C, Djafari-Rouhani B, Duval F, Dubus B, Pennec Y, et al. Waveguiding in two-dimensional piezoelectric phononic crystal plates. J Appl Phys 2007;101(11):114904. https://doi.org/10.1063/1.2740352.

[45] Tian Z, Yu L. Rainbow trapping of ultrasonic guided waves in chirped phononic crystal plates. Sci Rep 2017;7(1). https://doi.org/10.1038/srep40004.

[46] Kafesaki M, Sigalas MM, García N. Frequency modulation in the transmittivity of wave guides in elastic-wave band-gap materials. Phys Rev Lett 2000;85(19):4044–7.

[47] Cheng W, Wang J, Jonas U, Fytas G, Stefanou N. Observation and tuning of hypersonic bandgaps in colloidal crystals. Nat Mater 2006;5(10):830–6.

[48] Fleury R, Monticone F, Alù A. Invisibility and cloaking: Origins, present, and future perspectives. Phys Rev Appl 2015;4(3). https://doi.org/10.1103/PhysRevApplied.4.037001.

[49] Zhu X, Liang B, Kan W, Zou X, Cheng J. Acoustic cloaking by a superlens with single-negative materials. Phys Rev Lett 2011;106(1). https://doi.org/10.1103/PhysRevLett.106.014301.

[50] Maldovan M. Sound and heat revolutions in phononics. Nature 2013;503(7475):209–17.

[51] Chen T, Pauly M, Reis PM. A reprogrammable mechanical metamaterial with stable memory. Nature 2021;589(7842):386–90.

[52] Kolewe ME, Park H, Gray C, Ye X, Langer R, Freed LE. 3D structural patterns in scalable, elastomeric scaffolds guide engineered tissue architecture. Adv Mater 2013;25(32):4459–65.

[53] Sanders ED, Pereira A, Paulino GH. Optimal and continuous multilattice embedding. Sci Adv 2021;7(16). https://doi.org/10.1126/sciadv.abf4838.

[54] Xu S, Shen J, Zhou S, Huang X, Xie YM. Design of lattice structures with controlled anisotropy. Mater Des 2016;93:443–7.

[55] Cho H, Weaver JC, Pöselt E, in't Veld PJ, Boyce MC, Rutledge GC. Engineering the mechanics of heterogeneous soft crystals. Adv Funct Mater 2016;26(38):6938–49.

[56] Aquino J, Duarte I, Dias-de-Oliveira J. Modelling and effective properties prediction of metal foams. Sci Technol Mater 2018;30(1):43–9.

[57] Soyarslan C, Blümer V, Bargmann S. Tunable auxeticity and elastomechanical symmetry in a class of very low density core-shell cubic crystals. Acta Mater 2019;177:280–92.

[58] Gorishnyy T, Maldovan M, Ullal C, Thomas E. Sound ideas. Phys World 2005;18(12):24–9.

[59] Danielsson M, Parks DM, Boyce MC. Three-dimensional micromechanical modeling of voided polymeric materials. J Mech Phys Solids 2002;50(2):351–79.

[60] Danielsson M, Parks DM, Boyce MC. Micromechanics, macromechanics and constitutive modeling of the elasto-viscoplastic deformation of rubber-toughened glassy polymers. J Mech Phys Solids 2007;55(3):533–61.

[61] Nye JF. Physical properties of crystals: their representation by tensors and matrices. Oxford University Press; 1985.

[62] Thomas TY. On the stress-strain relations for cubic crystals. Proc Natl Acad Sci 1966;55(2):235–9.

[63] Ting T, Barnett D. Negative Poisson's ratios in anisotropic linear elastic media; 2005.

[64] Tilli M, Haapalinna A. Chapter 1 – Properties of silicon. In: Tilli M, Motooka T, Airaksinen V-M, Franssila S, Paulasto-Kröckel M, Lindroos V, editors. Handbook of silicon based MEMS materials and technologies. 2nd ed. Boston: William Andrew Publishing; 2015. p. 3–17.

[65] Brillouin L. Wave propagation in periodic structures: electric filters and crystal lattices. Courier Corporation; 2003.

[66] Babaee S, Shim J, Weaver JC, Chen ER, Patel N, Bertoldi K. 3D Soft metamaterials with negative Poisson's ratio. Adv Mater 2013;25(36):5044–9.

[67] Rothenburg L, Berlin AA, Bathurst RJ. Microstructure of isotropic materials with negative Poisson's ratio. Nature 1991;354(6353):470–2.

[68] Draper NR, Smith H. Applied regression analysis. John Wiley & Sons; 1998.

[69] Deshpande VS, Ashby MF, Fleck NA. Foam topology: bending versus stretching dominated architectures. Acta Mater 2001;49(6):1035–40.

[70] Jiang H, Coomes A, Zhang Z, Ziegler H, Chen Y. Tailoring 3D printed graded architected polymer foams for enhanced energy absorption. Compos B Eng 2021;224:109183. https://doi.org/10.1016/j.compositesb:2021.109183.